On the Tribological Properties of RGO-MoS$_2$ Composites Surface Modified by Oleic Acid

TianXia LIU (✉ 2005053@nun.edu.cn)

North Minzu University

jian Qin

North Minzu University

Jian Wang

North Minzu University

jing Li

North Minzu University

Abstract

Purpose To study the effect of oleic acid surface modified RGO/MoS$_2$ composite lubricating additives on the friction and wear properties of 10$^\#$ White Oil (10$^\#$ WO).

Method The influence of different concentrations of reduction graphene oxide/molybdenum disulfide (RGO-MoS$_2$) and oleic acid surface modified reduction graphene oxide/molybdenum disulfide (OA-RGO-MoS$_2$) on the lubricating properties in 10$^\#$ WO was investigated by using a four-ball long-term friction and wear tester. The microscopic morphology, lattice structure, composition and element valence of the prepared material were characterized by scanning electron microscope, Raman spectroscopy, X-ray diffractometer, X-ray photoelectron spectroscopy, element analyzer and other instruments. The diameter, structure, morphology, composition and element valence state of the wear scar were obtained by multifunctional universal tool microscope, scanning electron microscope and X-ray photoelectron spectroscopy.

Result In the RGO-MoS$_2$ white oil system, when 0.4 wt% RGO-MoS$_2$ was added, the anti-friction effect was the best, and the average friction coefficient (AFC) reduced by 21.8%. When 0.2 wt% RGO-MoS$_2$ was added, the anti-wear effect was the optimal, and the average wear scar diameter (AWSD) decreased by 12.4%. In the OA-RGO-MoS$_2$ white oil system, when 0.2 wt% OA-RGO-MoS$_2$ was added, the anti-friction and anti-wear effects were the best, and the AFC reduced by 33.3%, and AWSD reduced by 14.1%.

Conclusion Compared with RGO-MoS$_2$, OA-RGO-MoS$_2$ has a higher degree of graphitization, larger interlayer spacing, lower degree of layered accumulation, higher MoS$_2$ load, and weaker thermal stability. Both lubricating additives have good anti-friction and anti-wear effects at low concentrations, and the anti-friction and anti-wear effects are more prominent after being modified by oleic acid. Analysis of friction mechanism shows that a lubricating protective film containing iron, oxygen, molybdenum, carbon, and sulfur is formed through adsorption or tribochemical reaction during the friction process, which improves the lubrication state and plays a role in reducing friction and anti-wear.

1. Introduction

As a typical transition metal sulfide, MoS$_2$ is easy to slip between layers due to its unique two-dimensional layered structure and weak Van der Waals force between layers, which shows an excellent anti-friction effect and has been widely used in the field of lubrication [1–5]. The main preparation methods of molybdenum disulphide including mechanical stripping, liquid stripping, low-energy spherical disk combined with ultrasonic stripping, chemical vapor deposition, surfactant-assisted method, and hydrothermal method. Among them, the hydrothermal method is much more convenient and flexible, which has different morphologies and structures of molybdenum disulfide according to the different molybdates and vulcanizing agents (such as thiourea and sodium sulfide) in different reaction temperatures, pressure and under different acidity of reactants. However, some studies have found that MoS$_2$ nanoparticles are easy to be oxidized and have poor dispersibility in the base oil, leading to

agglomeration, which leads to the decrease of friction reduction and anti-wear level [6–7]. Therefore, looking for a good carrier material and preparing a new composite material with MoS_2 will provide new ideas for solving the above problems.

Due to its low interlaminar shear force and high elastic modulus, graphene has been widely concerned by the frictional field due to its excellent lubricity and load-bearing properties [8–11]. There are many studies on the preparation of carbon/molybdenum disulfide composites using graphite, carbon fibers, and carbon nanotubes as carrier materials as lubricating additives [12–13]. Graphite can be dispersed by oxidation intercalation to form graphene oxide (GO) with a low stacking degree. Lipophilic reduced graphene oxide (RGO) can be prepared by further reduction modification. RGO has a two-dimensional layered structure similar to MoS_2, but rich in heteroatom defect sites [14], with high specific surface area, low density, and good lipophilicity [15]. In recent years, it has been reported that reduced graphene oxide/molybdenum disulfide (RGO-MoS_2) materials were prepared by vapor deposition [16], hydrothermal [17], solvothermal [18], solution reduction [19], and microwave synthesis [20], with emphasis on the modulation of MoS_2 nanostructures. Therefore, taking advantage of the structural similarity of these two, taking the defect site of RGO as the anchoring site and loading MoS_2, it is expected to obtain the lubricant additive of RGO-MoS_2 with higher dispersibility.

It is effective method to improve the dispersity and dispersion stability of graphene-supported MoS_2 composites by introducing lipophilic group surface modified by modifiers. In this article, using thiourea as sulfur source and oleic acid as a modifier, the oleic acid-modified graphene oxide/molybdenum disulfide composite (OA-RGO-MoS_2) was prepared by hydrothermal reaction. The functional groups, elemental composition, morphology, and structure of OA-RGO-MoS_2 composites were characterized by several analytical instrument. The tribological properties of 10# white oil (10# WO) containing OA-RGO-MoS_2 and RGO-MoS_2 were studied on four-ball friction and wear tester, and its composite lubrication effects were discussed.

2. Experimental Section

2.1 Experimental equipment and reagents

Nanometer graphite powder and nanometer molybdenum disulfide powder were purchased from Shanghai Chaowei Nano Technology Co, Ltd. 10# white oil was bought from Kunshan Ximo Lubrication Technology. Oleic acid (OA), hydrazine hydrate, thiourea, ammonium molybdate, acetone, and ethanol were bought from Sinopharm Chemical Reagent Co., Ltd. and they are all analytical pure

The hydrothermal reactor (100 ml) was purchased from Anhui Kemi Instrument Co., Ltd. Steel ball (φ = 12.7 mm) was bought from Sinopec Petro chemical Scientific Research Institute. The MRS-10F four-ball friction and wear testing machine was manufactured by Jinan hengxu testing machine technology Co. Ltd.

2.2 Preparation of composites

The composite preparation process can be seen in figure 1. The process can now be reformulated with more detail as follows.

Preparation of RGO: GO was prepared by a modified Hummers method [21]. Firstly, configured GO dispersion liquid (20 mg/ml), took 20 ml dispersion liquid in a conical flask, and slowly added 2 ml hydrazine hydrate. Then, the conical flask was heated and reacted in an oil bath at 80 °C for 8 hours. Respectively washed with ethanol and deionized water three times and then centrifuged for 30 min under the condition of 7000 r/min, put it into the drying oven, and dried it at 80 °C for 12 hours toget black reduced graphene oxide (RGO) powder. Grinded it evenly and store it for standby.

Preparation of RGO-MoS$_2$: 20 ml GO dispersion liquid (20 mg/ml) was decanted in a conical flask, added 1 g ammonium molybdate and 2 g thiourea, and carried out ultrasonic treatment for 30 min. Then 2 ml hydrazine hydrate was added to the mixture and transferred to the hydrothermal reactor, which was heated and reacted at 180 °C for 24 h. After natural cooling in the hydrothermal reactor, respectively washed with ethanol anddeionized water three times and then centrifuged for 30 min under the condition of 7000 r/min. Put it into the drying oven, and dried it at 80 °C for 12 hours to get black RGO-MoS$_2$ powder. Grinded it evenly and store it for standby.

Preparation of OA-RGO-MoS$_2$: Adopt a preparation method similar to RGO-MoS$_2$, and added 60 ml of ethanol oleic acid solution (containing 4 ml of oleic acid) in the hydrothermal reaction process.

2.3 Preparation of 10$^{\#}$ WO+RGO-MoS$_2$ and 10$^{\#}$ WO+OA-RGO-MoS$_2$ oil samples

RGO-MoS$_2$ or OA-RGO-MoS$_2$ with a mass fraction of 0.2 wt%, 0.4 wt%, 0.6 wt%, 0.8wt % and 1.0 wt% were added to 10$^{\#}$ WO respectively. The specific configuration scheme was shown in Table 1 and Table 2. The above samples were magnetically stirred for 20 min and then dispersed by ultrasound for 1 h to prepare 10$^{\#}$ WO+ RGO-MoS$_2$ oil samples and 10$^{\#}$ WO+ OA-RGO-MoS$_2$ oil samples.

Table 1

$10^{\#}$ WO+RGO-MoS$_2$ oil sample preparation scheme

Serial number	Configure concentration(RGO-MoS$_2$ wt%)	Configuration
1#	0	20.0g $10^{\#}$ WO
2#	0.2	19.96g $10^{\#}$ WO+0.04g RGO-MoS$_2$
3#	0.4	19.92g $10^{\#}$ WO+0.08g RGO-MoS$_2$
4#	0.6	19.88g $10^{\#}$ WO+0.12g RGO-MoS$_2$
5#	0.8	19.84g $10^{\#}$ WO+0.16g RGO-MoS$_2$
6#	1.0	19.80g $10^{\#}$ WO+0.20g RGO-MoS$_2$

Table 2

$10^{\#}$ WO+OA-RGO-MoS$_2$ oil sample preparation scheme

Serial number	Configure concentration(OA-RGO-MoS$_2$ wt%)	Configuration
1#	0	20.0g $10^{\#}$ WO
2#	0.2	19.96g $10^{\#}$ WO+0.04g OA-RGO-MoS$_2$
3#	0.4	19.92g $10^{\#}$ WO+0.08g OA-RGO-MoS$_2$
4#	0.6	19.88g $10^{\#}$ WO+0.12g OA-RGO-MoS$_2$
5#	0.8	19.84g $10^{\#}$ WO+0.16g OA-RGO-MoS$_2$
6#	1.0	19.80g $10^{\#}$ WO+0.20g OA-RGO-MoS$_2$

2.4 Tribological experiments of $10^{\#}$ WO+RGO-MoS$_2$ and $10^{\#}$ WO+OA-RGO-MoS$_2$ oil samples

With the help of the MRS-10F four-ball friction and wear testing machine, the tribology experiment of $10^{\#}$ WO+RGO-MoS$_2$ oil sample and $10^{\#}$ WO+OA-RGO-MoS$_2$ oil sample was carried out with the GCr 15 special

steel ball (φ = 12.7 mm) for four-ball friction and wear testing machine. Four-ball friction and wear experiments were carried out under the conditions of test force 196 N, rotating speed 1200 r/min, time 0.5 h, and normal temperature.

2.5 Analytical methods

The morphology and structure of the composites had been analyzed by scanning electron microscope (SEM, Zeiss evo 10) and high-resolution transmission electron microscope (HRTEM, HT 7700, JEOL). The structural composition and graphitization degree of RGO-MoS$_2$ and OA-RGO-MoS$_2$ were characterized by X-ray diffraction (XRD, SmartlabSE, Rigaku) and laser Raman spectroscopy (Thermo Fisher). The elemental compositions of RGO-MoS$_2$ and OA-RGO-MoS$_2$ were executed on an elemental analyzer (Vario El cube, German elemental analysis company). The surface element contents and valence states of RGO-MoS$_2$ and OA-RGO-MoS$_2$ were obtained with a Thermo Fisher X-ray photoelectron spectroscopy (XPS, ESCALAB Xi+). The thermal stability and load of the composites were analyzed by a synchronous thermal analyzer (sta449f5, Netzsch, Germany). The analysis conditions were as follows: air atmosphere, heating rate of 10 °C/min, room temperature to 700 °C. SEM was used to analyze the surface morphology of the upper ball after friction and wear. The valence states of elements on the surface of the upper ball after friction and wear experiments were detected by XPS.

3. Results And Discussion

3.1 Morphology and structure for RGO-MoS$_2$ and OA-RGO-MoS$_2$

Fig. 2 shows the morphology of RGO-MoS$_2$ and OA-RGO-MoS$_2$ composite materials. As shown in Fig. 2 (a), (b) TEM images, and (e), (f) shown in SEM topography, MoS$_2$ is in the shape of nano-flower balls and is wrapped in slightly wrinkled, tulle-like RGO. The surface of the nanosphere is relatively smooth, and the flakes overlap each other and grow in all directions, and the oleic acid modified of RGO layer surface more smooth level off. MoS$_2$ is highly dispersed on the lamellar RGO, mainly because MoS$_2$ and RGO have similar two-dimensional layered structure, and RGO plays a role of nucleus and epitaxial growth substrate in the formation of molybdenum disulfide. Under this kind of hydrothermal conditions, GO is gradually reduced to RGO, while MoS$_2$ precursor is adsorbed on the defect position on the surface of RGO and reacts with the vulcanizing agent and a reducing agent to nucleate, and then molybdenum disulfide is attached to RGO for epitaxial growth to form a layer [22]. The HRTEM images in Fig. 2 (c) and (d) can intuitively display the layered structure of RGO-MoS$_2$ and OA-RGO-MoS$_2$ composites. The lattice spacing of the MoS$_2$ (002) crystal plane of the RGO-MoS$_2$ composite is about 0.67 nm, and the OA-RGO-MoS$_2$ material is about 0.70 nm, its slightly increase after OA modification. According to the above analysis, RGO-MoS$_2$ composite was successfully prepared by the hydrothermal method.

XRD spectra of RGO-MoS$_2$ and OA-RGO-MoS$_2$ are shown in Fig. 3. It can be seen from the figure 3 that the two diffraction peaks of 2θ=23.3 ° and 2θ=43.1 ° belong to the (002) and (100) lattices of graphene respectively. The diffraction peaks near 33.5 ° and 57.4 ° belong to (100) and (110) planes of MoS$_2$,

respectively. The diffraction peaks of OA-RGO-MoS$_2$ and RGO-MoS$_2$, which belong to the (002) crystal plane of MoS$_2$, appear at 13.2 ° and 13.7 ° respectively, which is inconsistent with the interlayer spacing of standard MoS$_2$ (002) diffraction peak at 14.4° (0.62 nm). This phenomenon is attributed to MoS$_2$ material with low stacking degree and extended layer spacing synthesized by hydrothermal reaction [23-24]. Compared with MoS$_2$, the (002) crystal plane of the two has a low angle shift, and the (002) crystal plane was the position of the S-Mo-S layer of molybdenum disulfide, and its peak intensity is proportional to the stacking degree of lamellae. The MoS$_2$ (002) peak strength of OA-RGO-MoS$_2$ is weaker than that of RGO-MoS$_2$. It indicates that the layered stacking degree of OA-RGO-MoS$_2$ is inferior to the RGO-MoS$_2$. RGO-MoS$_2$ (002) crystal plane of OA-RGO-MoS$_2$ shifts to a lower angle, indicating that the layer spacing of OA-RGO-MoS$_2$ is larger than that of RGO-MoS$_2$ after modification by OA. In other words, the successful insertion of the O atom into the MoS$_2$ skeleton causes the interlayer expansion of S-Mo-S, which leads to the increase of interlayer spacing of composite materials [25]. This result is consistent with SEM and HRTEM.

To further characterize the structure and composition of the composite nanomaterials, Raman spectroscopy was used to analyze the composite nanomaterials. Fig. 4 displays the Raman spectra of RGO, RGO-MoS$_2$ and OA-RGO-MoS$_2$. The peaks near 1347 cm^{-1}nd 1579 cm^{-1} correspond to the D peak of sp^3 hybrid disordered carbon or defective carbon and the G peak of sp^2 hybrid fossil ink carbon respectively. Generally speaking, the ratio of peak intensity I$_D$/I$_G$ represents the defect degree of carbon materials. I$_D$/I$_G$ of RGO is 1.1234, that of OA-RGO-MoS$_2$ is 1.1845, and that of RGO-MoS$_2$ is 1.2137. The I$_D$/I$_G$ values of RGO-MoS$_2$ and OA-RGO-MoS$_2$ are higher than those of RGO, indicating that the volume of sp^2 atom decreases in the redox process. It shows that the hydrothermal reaction reduces the graphene oxide to a greater extent [26]. The value of I$_D$/I$_G$ of OA-RGO-MoS$_2$ is lower than that of RGO-MoS$_2$, which indicates that its graphitization degree is higher and its surface defects are reduced, which is beneficial to improving its tribological properties [27].

RGO-MoS$_2$ and OA-RGO-MoS$_2$ shown E$^1_{2g}$ and A$_{1g}$ characteristic Raman peaks of MoS$_2$ near 374 cm^{-1} and 400 cm^{-1}, respectively, while the E$^1_{2g}$ and A$_{1g}$ characteristic Raman peaks of MoS$_2$ were not observed in RGO. The research shows that the stronger peak value of A$_{1g}$, the stronger van der waals force between MoS$_2$ layers is [28]. It can be seen that the van der Waals force between MoS$_2$ layers in OA-RGO-MoS$_2$ is weaker than RGO-MoS$_2$. Due to the weak interaction force between layers, MoS$_2$ is proned to slide between layers during friction, showing excellent lubrication performance.

4.2 Thermogravimetric analysis of RGO-MoS$_2$ and OA-RGO-MoS$_2$

In an air atmosphere, the thermogravimetric analysis results of MoS$_2$, RGO, RGO-MoS$_2$, and OA-RGO-MoS$_2$ are shown in Fig. 5. The component mass ratio of the composite material is calculated by the mass percentage of the sample at 700 °C. The calculation formula is [29]:

$$W_{MoS_2} \times X_{MoS_2} + W_{RGO} \times (1 - X_{MoS_2}) = W_{MoS_2/RGO}$$

The result data are shown in Table 3 。

Table 3 TGA data of MoS_2, RGO, RGO-MoS_2 and OA-RGO-MoS_2

Sample	Residual mass ratio wt %	MoS_2 wt %	RGO wt %
MoS_2	86.0	/	/
RGO	2.6	/	/
RGO-MoS_2	60.0	56.7	43.3
OA-RGO-MoS_2	64.0	63.3	36.7

Combined with table 3 and Fig. 5 (a), it can be seen that RGO-MoS_2 and OA-RGO-MoS_2 are heated and burned in the air atmosphere, and the remaining mass is 60.0% and 64.0% respectively. The MoS_2 is heated in an air atmosphere and undergoes an oxidation reaction, and some S atoms are replaced by O atoms, thus reducing the mass. The vast majority of RGO is oxidized to CO_2 by heating and combustion, and only a small part of amorphous carbon is difficult to be oxidized, so there is still 2.6% mass residue after 700 °C. The MoS_2 loading in RGO-MoS_2 and OA-RGO-MoS_2 composites is calculated to be 56.7% and 63.3% respectively. The weight loss rate of RGO-MoS_2 is higher than that of OA-RGO-MoS_2. The reason is that OA-RGO-MoS_2 is modified by oleic acid, which makes the RGO carrier load more MoS_2. Because MoS_2 has good thermal stability, it only loses a small amount of mass when heated and burned in the air atmosphere. Therefore, the weight loss rate of OA-RGO-MoS_2 loaded with more MoS_2 is lower than that of RGO-MoS_2, and first reach a stable mass around 550 °C.

It can be seen from Fig. 5 that the adsorption water is mainly removed at about 100 °C, the main mass loss is attributed to the decomposition of unstable oxygen-containing functional groups between 100 °C to 250 °C, and the decomposition of relatively stable oxygen-containing functional groups between 250 °C to 450 °C. Mass loss from 450 °C to 600 °C is ascribed to RGO combustion. The maximum mass-loss rates of OA-RGO-MoS_2 and RGO-MoS_2 are 2.865 %/min and 2.067 %/min, respectively, and the temperature at this time is 497.13 °C and 524.56 °C, respectively. The analysis reason is that after OA modification, more organic functional groups are grafted on the surface of OA-RGO-MoS_2, and it is more fully heated and burned in the air atmosphere, which also indicates the thermal stability of RGO-MoS_2 is better than that of OA-RGO-MoS_2.

4.3 Elemental analysis of RGO-MoS_2 and OA-RGO-MoS_2

To quantitatively analyze the kinds and contents of elements in RGO-MoS_2 and OA-RGO-MoS_2, a comprehensive analysis is made by using an element analyzer (total element content) and XPS (surface

element content). The elemental analysis of RGO-MoS$_2$ and OA-RGO-MoS$_2$ is shown in table 4. Table 4 XPS surface content data shows that the content of C, O, and Mo in OA-RGO-MoS$_2$ is higher than that in RGO-MoS$_2$, while the content of the S element is lower than that in RGO-MoS$_2$. The content of C and H elements in OA-RGO-MoS$_2$ is higher than that in RGO-MoS$_2$, and the content of S and N elements is lower than that in RGO-MoS$_2$. The increase of molybdenum and oxygen content may be due to OA modification of OA-RGO-MoS$_2$, which leads to more MoS$_2$ being loaded on the RGO carrier. A large number of O atoms are inserted into the skeleton of molybdenum disulfide, resulting in a Mo-O bond, which leads to the expansion of the S-Mo-S interlayer. And H and N mainly come from -COOH and -OH in OA or NH$_4^+$ in raw material ammonium molybdate. The experimental results are in good agreement with XRD, XPS, and TG analysis results.

Table 4 Elemental analysis results of RGO-MoS$_2$ and OA-RGO-MoS$_2$

Sample	XPS				Elemental analyzer			
	C/ %	O/ %	S/ %	Mo/ %	C/ %	S/ %	H/ %	N/ %
RGO-MoS$_2$	29.94	16.66	33.21	20.19	13.20	29.76	0.91	1.94
OA-RGO-MoS$_2$	32.02	17.53	29.78	20.67	17.33	24.80	0.94	1.83

4.4 XPS analysis of RGO-MoS$_2$ and OA-RGO-MoS$_2$

Fig. 6 shows the XPS spectra of RGO-MoS$_2$ and OA-RGO-MoS$_2$. For C1s spectra (a) and (e), the peak located at 284.8 eV belongs to the C-C bond; The characteristic peaks located at 285.96 eV and 286.39 eV belong to C-O-C and C-O; The characteristic peaks located at 288.53 eV and 288.71 eV belong to O-C=O and C=O.

For O1s spectra (b) and (f), the characteristic peaks located at 530.43 eV or 530.95 eV are ascribed to Mo-O. The binding energy peaks of C-O-C and C-O are located at 531.50 eV and 532.04 eV, respectively belong to; The peaks located at 532.69 eV and 533.40 eV are attributed to O-C=O and C=O. It can be seen from the figure that, after OA modification, the content of the Mo-O bond increases. Mo-O bond mainly comes from the insertion of O atoms into the MoS$_2$ skeleton, which causes the interlayer expansion of S-Mo-S and further increases the interlayer spacing of composite materials. This result also verifies the XRD analysis.

For S2p spectra (c) and (g), the peaks located at 161.22 eV and 161.92 eV belong to S2p$_{3/2}$ orbit. The binding energy at 162.42 eV and 163.14 eV belong to S2p$_{1/2}$ orbit, indicating that S element mainly exists in the form of S^{2-} in the composite.

For Mo3d spectra (d) and (h), the peaks located at 228.25 eV and 229.01 eV belong to Mo3d$_{5/2}$ orbit. The peaks located at 231.73 eV and 232.16 eV belong to the Mo3d$_{3/2}$ orbit. The peaks located at 225.67 eV and 226.44 eV belong to S2s orbit. This indicates that the Mo element mainly exists in the form of Mo^{4+}.

In addition, characteristic peaks located at 235.19 eV and 236.09 eV belong to Mo^{6+} and are mainly formed by oxidation on the surface of products in the air [30-31].

4.5 Tribological properties of $10^\#$ WO+RGO-MoS$_2$ and $10^\#$ WO+OA-RGO-MoS$_2$ oil samples

Fig. 7 shows the friction coefficient (FC) variation with time diagram of RGO-MoS$_2$ and OA-RGO-MoS$_2$ oil samples with different mass fractions. Fig. 8 shows the average friction coefficient (AFC) variation with additive content diagram of RGO-MoS$_2$ and OA-RGO-MoS$_2$ oil samples. Combined with Fig. 7 (a) and Fig. 8, it can be seen that AFC first declined and then increased with the increase of the added concentration of RGO-MoS$_2$ in $10^\#$ WO. When 0.4 wt% RGO-MoS$_2$ is added, FC was significantly lower than that of blank $10^\#$ WO, and the running-in period is shorter and the curve trend was relatively stable. At this time, AFC is 0.068, 21.8% lower than that of $10^\#$ WO (0.087). This may be because a small amount of RGO-MoS$_2$ entered the friction interface, and gradually adsorbed on the surface of the contact surface micro-concave, fill the micro-pits of the friction interface, friction chemical reaction occurs in the friction process and then form a complex lubricating film to reduce friction effect. After increasing the concentration of RGO-MoS$_2$, AFC began to rise gradually. When 1.0 wt% is added, AFC is 0.096, which is 10.3% higher than that of $10^\#$ WO. In addition, the curve fluctuated sharply, the run-in period is longer, and the anti-friction effect is not obvious. This may be because RGO-MoS$_2$ with a higher added concentration is easy to aggregate into large particles in $10^\#$ WO, which breaks through the oil film thickness and enters the friction interface to form abrasive wear, failing to achieve the effect of friction reduction.

From Fig. 7 (b) and Fig. 8, It can be seen that AFC decreases first and then increases after OA-RGO-MOS$_2$ is added. AFC of all oil samples added with OA-RGO-MOS$_2$ is less than that of pure $10^\#$ WO, and the curve is relatively stable. The reason may be that the expansion of layer spacing reduces the inter-layer interaction. Thus, the anti-friction performance of the material is improved. When 0.2 wt% OA-RGO-MOS$_2$ is added, the friction reduction effect is the best. The AFC is 0.058, 33.3% lower than that of pure $10^\#$ WO. When 0.6 wt% and 0.8 wt% are added, the AFC is almost the same, 0.07556 and 0.07548 respectively. However, it is obvious from Fig. 7 (b) that the FC curve of 0.8 wt% has a more obvious upward trend after 1000 s. At 1.0 wt%, the AFC of OA-RGO-MoS$_2$ is 0.085, which is lower than that of RGO-MoS$_2$ (0.096) at this concentration, indicating that after OA modification, the dispersion of OA-RGO-MoS$_2$ in $10^\#$ WO become better for the surface grafting of oleophilic groups. Even in a larger concentration, it is not easy to aggregate, and because OA-RGO-MoS$_2$ is adsorbed on the interface of friction pair, it participates in the formation of lubricating film and enhances the strength of oil film, thereby to reduce friction [32].

4.6 Effects of RGO-MoS$_2$ and OA-RGO-MoS$_2$ on wear

After the friction and wear experiment, removed the steel ball and ultrasonically cleaned for 30 min in a beaker containing acetone. After it is naturally dried, using a universal tool microscope to photograph the scar morphology of the test ball and measure its wear scar diameter, to observe the change of wear amount with the increase of additive concentration. The average wear scar diameter(AWSD) variation

with additive content and the wear scar morphology are shown in Fig. 9. Fig. 9 shows that the wear scar of the lower test ball after rubbing the oil sample of OA-RGO-MoS$_2$ are shallower and narrower than those of RGO-MoS$_2$. With the increase of RGO-MoS$_2$ and OA-RGO-MoS$_2$ addition concentration, the changing trend of the AWSD of steel balls is firstly declined and then increased. On the other hand, when the concentration of RGO-MoS$_2$ is 0.2 wt%, the AWSD decreases to 0.559 mm, which is 12.4% lower than the AWSD of 10$^\#$ WO of 0.638 mm. The AWSD of OA-RGO-MoS$_2$ at 0.2 wt%, 0.4 wt%, and 0.6 wt% is 0.548 mm, 0.550 mm, and 0.551 mm, respectively. The minimum AWSD value is 14.1% lower than that of 10$^\#$ WO. If the concentration of OA-RGO-MoS$_2$ is 1.0 wt%, it can be easily seen that the diameter of the wear scar is obviously larger than that of 10$^\#$ WO. When the additive content is less than 1.0 wt%, compared with OA-RGO-MoS$_2$, OA-RGO-MoS$_2$ has smaller wear scar diameter, shallower and finer wear marks than RGO-MoS$_2$. The analysis reason may be that OA-RGO-MoS$_2$ has been modified by OA, and its physical and chemical properties are better. Moreover, it has lipophilic groups which are better to disperse in 10$^\#$ WO. Therefore, the wear resistance of RGO-MoS$_2$ is improved compared with that of unmodified RGO-MoS$_2$. Nevertheless, when the addition concentration is too higher, it is easier to form large agglomeration particles, break through the oil film thickness, form abrasive wear, and unable to play an anti-wear role.

4.7 Analysis of anti-friction and anti-wear mechanism

To explore the anti-friction and antiwear mechanism of RGO-MoS$_2$ and OA-RGO-MoS$_2$, the upper test balls with the best effects were selected after the friction experiment with the addition concentration of 0.2 wt%, the addition concentration of 1.0 wt% and the blank 10$^\#$ WO, which were characterized magnified 1000 times by SEM. From Fig. 10 (a) can see that under the lubrication of 10$^\#$ WO, the furrow on the wear scar surfaceis wide and irregular, and a large number of irregular peeling pits of adhesive wear appears on the surface of the wear mark, indicating that the wear mode is mainly adhesive wear. It can be seen from Fig. 10 (b) that when 0.2 wt% RGO-MoS$_2$ is added, the wear marks become thinner, shallower, and more regular, with a few peeling pits appear on the surface of the wear marks. It can be seen from Fig. 10 (c) that when 0.2 wt% OA-RGO-MoS$_2$ is added, the surface of wear marks is smooth and flat, without peeling pits, and the existence of wear marks can hardly be seen, which shows that OA-RGO-MoS$_2$ has more excellent anti-friction and anti-wear effects. It can be judge from Fig. 10 (d) and Fig.10 (e) that when the additive amount is 1.0 wt%, the furrows on the wear scar surface of increasing RGO-MoS$_2$ and OA-RGO-MoS$_2$ become thicker and denser. Meanwhile, the irregular spalling pits and agglomerated wear fragments were appeared. This indicates that the composite material has been added excessively, and the excessive composite material is converted into abrasive grains in the lubricating oil system, which increases the wear of abrasive grains and cannot play a role.

Table 5 Analysis of types and contents of wear trace elements on the surface of steel balls

Sample	Element content					
	C/ %	O/ %	S/ %	Cr/ %	Fe/ %	Mo/ %
0.2 wt% RGO-MoS$_2$	1.80	3.83	0.02	1.37	92.98	/
0.2 wt% OA-RGO-MoS$_2$	8.17	12.79	0.22	2.22	76.60	/
1.0 wt% RGO-MoS$_2$	6.32	7.39	/	0.96	85.18	0.15
1.0 wt% OA-RGO-MoS$_2$	9.17	7.26	/	1.62	81.68	0.27

Fig. 11 and Table 5 show the EDS analysis results of the wear scar surface of the steel ball. A friction film including C, O, Fe, and Cr elements is detected in the wear scar of all samples, among which Fe and Cr elements all are from the steel ball itself, and C and O elements stem from the lubricating film formed by the interaction of additives and lubricating oil during the friction process. At the same addition concentration, the content of C and O elements on the surface of wear scar with OA-RGO-MoS$_2$ is higher, while it is short of the content of Fe element. In addition, S and Mo elements appeared on the wear scar surface, which indicated that the additives participated in the friction chemical reaction occurred on the wear scar surface to form a friction reaction film. The proof of this result also can be found in the XPS analysis.

To further analyze the anti-friction and anti-wear mechanism of RGO-MoS$_2$ and OA-RGO-MoS$_2$, the XPS analysis carried out on the ware scar surface after friction test with the best anti-friction and anti-wear effect at the addition concentration of 0.2 wt%, and the results are shown in Fig. 12.

Fig. 12 (a) and Fig. 12 (f) are C1s spectra of wear scar on the surface of the upper test ball after adding 0.2 wt% RGO-MoS$_2$ and OA-RGO-MoS$_2$ to the WO for friction test.

The largest characteristic peak at 284.8 eV belongs to the C-C bond, and the middle characteristic peak at 285.20 eV or 285.26 eV belong to the C-O-C bond and C-O bond. The smallest peak at 288.16 eV or 288.18 eV belong to the O-C=O bond and C=O bond [33]. Its main source is organic matter in lubricating oil or lubricating film formed by the oil and additives during friction.

Fig. 12(b) and Fig. 12 (g) are O1s spectra of wear scar. The peaks of 529.84 eV or 530.03 eV belong to the metal oxides, mainly Fe oxides. The characteristic peaks near 531.34 eV-531.48 eV belong to the C-O bond and C-O-C bond. The peaks near 532.33 eV-532.73 eV belong to the C=O and O-C=O bond.

Fig. 12(c) and Fig. 12(h) are Fe2p spectra of wear scar. Among them, nearby 710.31 eV-710.38 eV peaks belong to the FeO characteristic peaks, while 711.19 eV-711.58 eV peaks belong to the Fe$_2$O$_3$ characteristic peaks, and 724.95 eV-725.34 eV neighbouring characteristic peaks belong to the Fe2p$_{1/2}$ orbit. The peak areas of FeO and Fe$_2$O$_3$ are designated as A1 and A2 respectively. By comparing the ratio of Fe^{2+} to Fe^{3+} (the area of A1 to A2 in the map), it can evaluate the wear situation of the steel ball surface [34-35]. When the content of RGO-MoS$_2$ is 0.2 wt%, A1:A2 in the map is 0.95. When the content of

OA-RGO-MoS$_2$ is 0.2 wt%, A1:A2 value is 1.28. The above results show that the anti-friction and anti-wear effect of OA-RGO-MoS$_2$ is better than that of RGO-MoS$_2$, and the addition of OA-RGO-MoS$_2$ to 10$^{\#}$ WO improves the anti-friction and anti-wear effect of lubricating oil.

Fig. 12(d) and Fig. 12 (l) are Mo3d spectra of wear scar. The peak of 232.30 eV or 232.46 eV belongs to the Mo-S bond, which indicates the existence of MoS$_2$ on the friction surface. The peak nearby 235.40 eV-235.61 eV belongs to the Mo-O bond of MoO$_3$, that is, Mo is oxidized during friction.

Fig. 12(e) and Fig. 12(j) are S2p spectra of wear scar. The feature peak at 162.68 eV-163.48 eV belongs to S^{2-} in MoS$_2$. The characteristic peak vicinity 168.15 eV-168.95 eV belongs to S^{6+}, which indicates that there is not only Fe oxide, but also FeSO$_4$ or Fe$_2$(SO$_4$)$_3$ on the surface of the wear scar. That is, S is oxidized during friction.

Based on the above analysis, the lubrication mechanism of composite materials as additives is put forward. Firstly, the additive enters the contact surface of the friction pair with 10$^{\#}$ WO, and under the action of higher contact pressure, the additive is adsorbed on the surface of the friction pair to form an adsorption protective film, which fills the defect areas such as micro cracks and micro pits on the surface of the friction pair, playing a role in repairing the worn surface during friction. Secondly, in the process of friction reaction, MoS$_2$ and RGO in the composite material play a synergistic lubricating effect, and a lubricating film containing iron oxide, iron sulfur oxide, molybdenum oxide, molybdenum disulfide and carbonaceous materials is formed on the surface of the friction pair, which avoids the direct contact of the friction pair and plays a role in reducing friction and antiwear. For RGO-MoS$_2$ and OA-RGO-MoS$_2$ composites, their sizes are smaller than the oil film thickness at low additive concentration, which can cause interlayer slip between friction interfaces and play a role in reducing friction. When the additive concentration is too high, excessive composite materials will agglomerate and turn into abrasive particles in the lubricating oil system, which breaks through the oil film thickness, increasing the wear of abrasive particles, and cannot play an anti-wear role. However, on the whole, OA-RGO-MoS$_2$ has better comprehensive lubricating performance.

5. Conclusion

1. Compared with RGO-MoS$_2$, OA-RGO-MoS$_2$ has a higher degree of graphitization, larger interlayer spacing, lower degree of layered accumulation, higher MoS$_2$ load, and weaker thermal stability.

2. OA-RGO-MoS$_2$ and RGO-MoS$_2$ have better anti-friction and anti-wear effects at lower additive concentration. Among them, the surface of OA-RGO-MoS$_2$ modified by OA is grafted with lipophilic groups, which has better lubricating performance and better improves the anti-friction and anti-wear performance of 10$^{\#}$ WO.

3. The analysis of friction mechanism shows that OA-RGO-MoS$_2$ and RGO-MoS$_2$ can form lubricating protective films containing with iron, oxygen, molybdenum, carbon and sulfur on the friction surface through adsorption and tribochemical reaction in the friction process, which improves the lubrication state of 10$^\#$ WO. Thus, it plays the role of friction reduction and wear resistance. On the whole, OA-RGO-MoS$_2$ has better comprehensive lubrication performance.

Declarations

Author contributions

Tianxia Liu and Jian Qin conceived and designed the experiments; Jian Qin performed the experiments; Tianxia Liu contributed reagents/materials and analysis tools; Jian Wang and Jing Li helped some results analysis and discussion; Jian Qin and Tianxia Liu wrote the paper.

Conflicts of interest

The authors declare that they have no competing interests.

Acknowledgements

References

1. R R SAHOO, S.K.B.I.S.W.A.S.: Effect of Layered MoS$_2$ nanoparticles on the frictional behavior and microstructure of lubricating greases[J]. Tribol. Lett. **53**(1), 157–171 (2014)

2. WEI LI CUI, SHAN SHAN XU, BO, Y.A.N., et al.: Triphasic 2D materials by vertically stacking laterally heterostructured 2H-/1T'-MoS$_2$ on Graphene for enhanced photoresponse[J]. Advanced Electronic Materials **3**(7), 1700024 (2017)

3. LEMBKE, D.O.N.I.N.I.K., BERTOLAZZI, S.I.M.O.N.E.: KIS ANDRAS. Single-layer MoS$_2$ electronics[J]. Acc. Chem. Res. **48**(1), 100–110 (2015)

4. Kunhong, Hu, Yong, Xu, Yufu, Xu, et al.: Tribological Properties of MoS$_2$ Lubricants with Different Morphologies in an Ionic Liquid[J]. Tribology **35**(02), 167–175 (2015)

5. Hu, K.H., Hu, X.G., Xu, Y.F., et al.: The effect of morphology on the tribological properties of MoS$_2$ in liquid paraffin[J]. Tribol. Lett. **40**(1), 155–165 (2010)

6. Hengzhou, W., Kunheng, Hu, Xianguo, Hu. Tribological properties of MoS$_2$ nanoparticles as additive in a machine Oil[J]. Tribology, 2004(01): 33–37

7. Bai Geling, Wu, Zhuangzhi: Synthesis and tribological properties of MoS_2 nanospheres[J]. Lubr. Eng. **38**(04), 93–96 (2013)

8. AGR AWAL N, PAR IHAR A S, SINGH J P, et al.: Efficient nanocomposite foMRation of acyrlo nitrile rubber by incorporation of graphite and graphene layers: reduction in friction and wear rate[J]. Procedia materials science **10**, 139–148 (2015)

9. BER MAN D, ER DEMIR A: ANIR UDHA V. Sumant Few layer graphene to reduce wear and friction on sliding steel surfaces[J]. Carbon **54**(54), 454–459 (2013)

10. SHI, Z., SHUM P W, W.A.S.Y.A., et al.: Tribological perfoMRance of few layer graphene on textured M2 steel surfaces[J]. Surface coatings technology **296**, 164–170 (2016)

11. DIANA, B., ERDEMIR, A., SUMANT A V, et al.: Reduced wear and friction enabled by graphene layers on sliding st-eel surfaces in dry nitrogen[J]. Carbon **59**(8), 167–175 (2013)

12. Zhang, X., Luster, B., Church, A., et al.: Carbon nanotube−MoS2 composites as solid lubricants[J]. Acs Applied Materials & Interfaces **1**(3), 735 (2009)

13. Wang Junxiang, Gu, Mingyuan, Z., Caizhen, et al.: Tribological properties of hybrid carbon fiber and MoS_2 peinforced polyamide 1010 composites[J]. Acta Materiae Compositae Sinica **20**(2), 13–18 (2003)

14. Fengzhi, T.A.N., Yanru, Z.H.A.O., Yafeng, C.A.O., et al.: Preparation of MoS_2/graphene and its performance for anode materials of Li-ion battery[J]. Chemical Industry and Engineering Progress **36**(12), 4519–4523 (2017)

15. Shiren, W.A.N.G., Yue, Z.H.A.N.G., Noureddine, A.B.I.D.I., et al.: Wettability and surface free energy of graphene films[J]. Langmuir **25**(18), 11078–11081 (2009)

16. Yumeng, S.H.I., Henan, L.I., Jen It, W.O.N.G., et al.: MoS2 surface structure tailoring via carbonaceous promoter[J]. Sci. Rep. **5**, 10378 (2015)

17. Ashish, B.A.H.U.G.U.N.A., Suneel, K.U.M.A.R., Vipul, S.H.A.R.M.A., et al.: Nanocomposite of MoS2-RGO as facile, heterogeneous, recyclable, and highly efficient green catalyst for one-pot synthesis of indole alkaloids[J]. ACS Sustainable Chemistry & Engineering **5**(10), 8551–8567 (2017)

18. MENG X Y, YU, L., MA, C., et al.: Three-dimensionally hierarchical MoS_2/graphene architecture for high-performance hydrogen evolution reaction[J]. Nano Energy **61**, 611–616 (2019)

19. Lan, Y.A.N.G., Xu-zhen, W.A.N.G., Yang, L.I.U., et al.: Monolayer MoS_2 anchored on reduced graphene oxide nanosheets for efficient hydrodesulfurization[J]. Appl. Catal. B **200**, 211–221 (2017)

20. Jinliang, L.I., Xinjuan, L.I.U., Likun, P.A.N., et al.: MoS$_2$-reduced graphene oxide composites synthesized via a microwave-assisted method for visible-light photocatalytic degradation of methylene blue[J]. RSC Advances **4**(19), 9647–9651 (2014)

21. JEONG H K,LEE Y P,L R J, et al.: Evidence of graphitic AB stacking order of graphite oxides[J]. J. Am. Chem. Soc. **130**(4), 1362–1366 (2008)

22. Zheng Anda, YangCheng: gong, Wang Donge, et al. Highly active MoS_2/reduced graphene oxide catalyst for anthracene hydrogenation[J]. Chemical Industry and Engineering Progress, 2020: 1–14

23. LI, MIN, WANG DONG E, LI JIA HE, et al.: Facile hydrotheMRal synthesis of MoS_2 nano-sheets with controllable structures and enhanced catalytic perfoMRance for anthracene hydrogenation[J]. RSC Advances **6**(75), 71534−71542 (2016)

24. LI, JIA HE, WANG DONG E, MA HUAI JUN, et al.: Ionic liquid assisted hydrotheMRal synthesis of MoS2 double-shell polyhedral cages with enhanced catalytic hydrogenation activities[J]. RSC Advances **7**(38), 23523−23529 (2017)

25. Ba Zhaowen, H., Guowei, Q.D., et al.: Preparation and tribological performance of RGO/MoS_2 as composite nano-additives[J]. Tribology **39**(02), 140−149 (2019)

26. Ma Zhanhui, Y., Jie, Z.: Zhenye et al. Mercury vapor sensor based on composites of MoS_2/Graphene [J]. Journal of Synthetic Crystals **49**(06), 1107−1111 (2020)

27. LI, B., ZHOU, L.: WU D, et al. Photochemical chlorination graphene[J]. ACS Nano **5**(7), 5957−5961 (2011)

28. LI, X., LI, J.H., WANG, K., et al.: Pressure and temperature-dependent Raman spectra of MoS_2 film[J]. Appl. Phys. Lett. **109**(24), 242101 (2016)

29. ZHOU, X., WAN L J, GUO, Y.G.: Synthesis of MoS_2 nanosheet-graphene nanosheet hybrid materials for stable lithium storage[J]. Chem. Commun. **49**(18), 1838−1840 (2013)

30. YANG, H., WANG, M., LIU, X., et al.: MoS_2 embedded in 3D interconnected carbon nanofiber film as a free-standing anode for sodium-ion batteries[J]. Nano Research **11**(7), 3844−3853 (2018)

31. Park, S.K., Lee, J., Bong, S., et al.: Scalable synthesis of few-layer MoS_2 incorporated into hierarchical porous carbon nanosheets for high-perfoMRance Li-and Na-ion battery anodes[J]. ACS applied materials interfaces **8**(30), 19456−19465 (2016)

32. Enzhu, Hu, Dongrun, Yu, Yuchao, T., et al.: Rice husk ceramic particles improving lubrication property of liquid paraffin[J]. Transactions of the Chinese Society of Agricultural Engineering **33**(10), 265−270 (2017)

33. Liu Tianxia, K., Kai, W.: Jian, et al. Effect of nano-LaF_3 on the granular flow lubrication behavior of biomass fuel soot[J]. Chemical Industry and Engineering Progress **39**(08), 3354−3361 (2020)

34. Zhao Jun, C.G., Yong, Y.H.Y., et al.: A novel route to the synthesis of an Fe_3O_4/h-BN 2D nanocomposite as a lubricant additive. RSC advances[J] **9**(12), 6583−6588 (2019)

35. ZHANG, Q.Q., Wu, B., Song, H.R., et al.: Preparation characterization and tribological properties of polyalphaolefin with magnetic reduced graphene oxide/Fe_3O_4[J]. Tribol. Int. **141**, 105952 (2020)

Figures
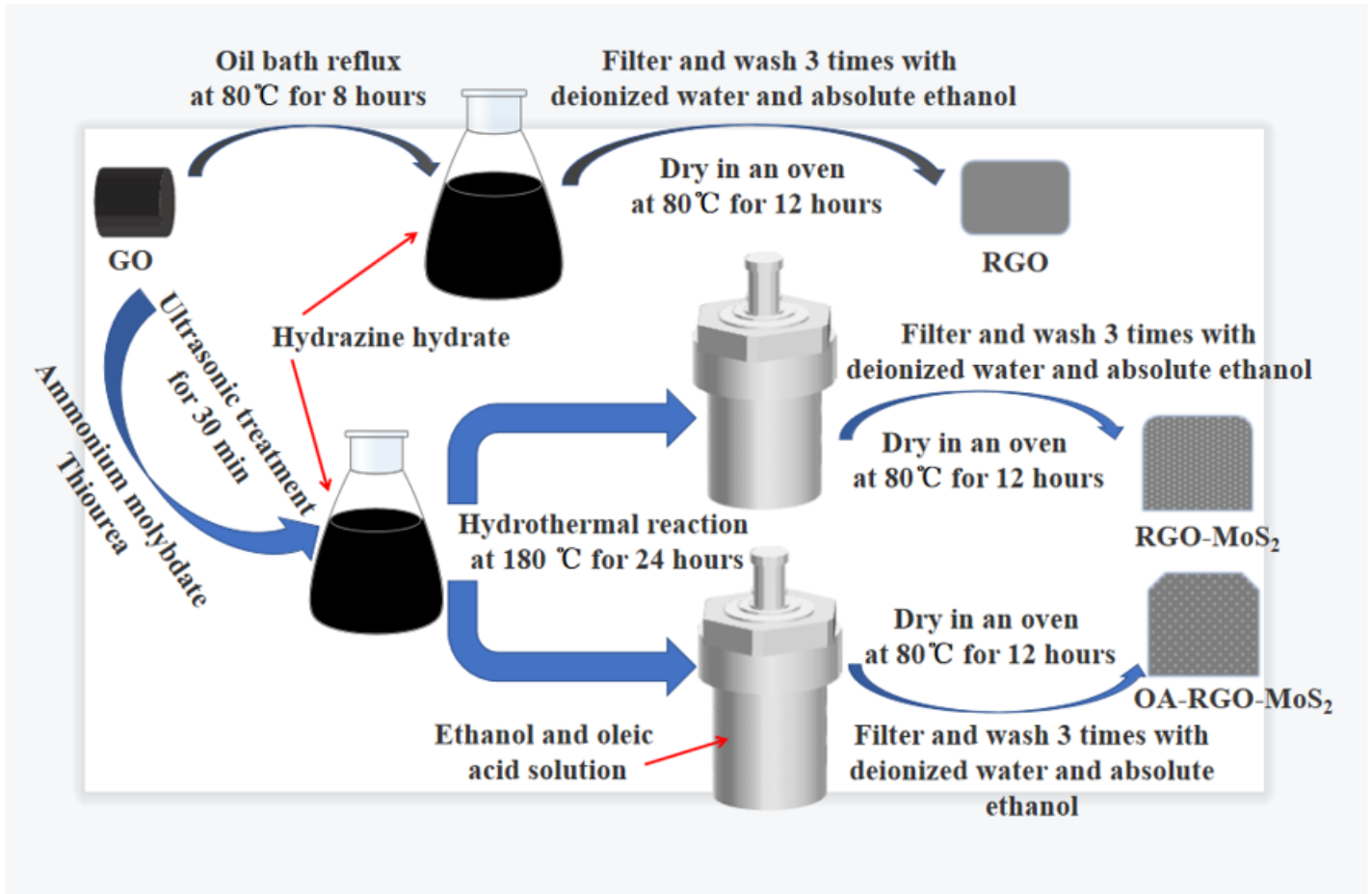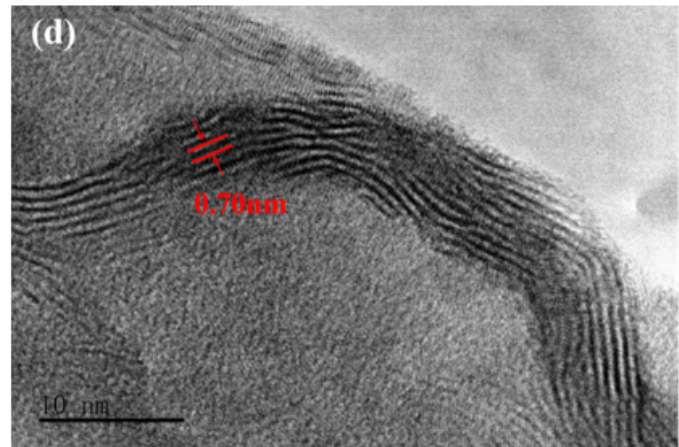
Figure 1

Flow chart of composite preparation
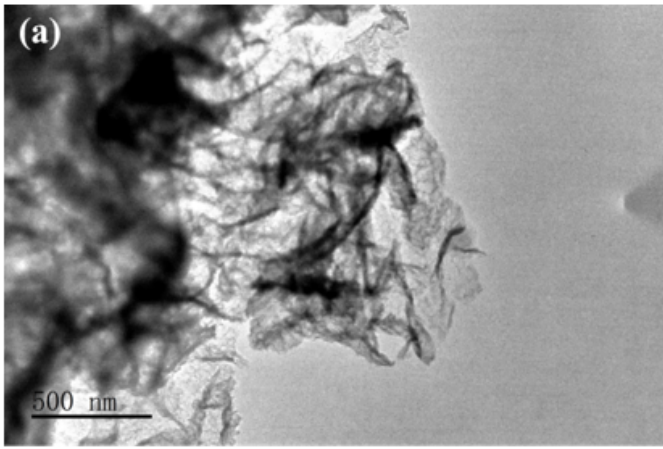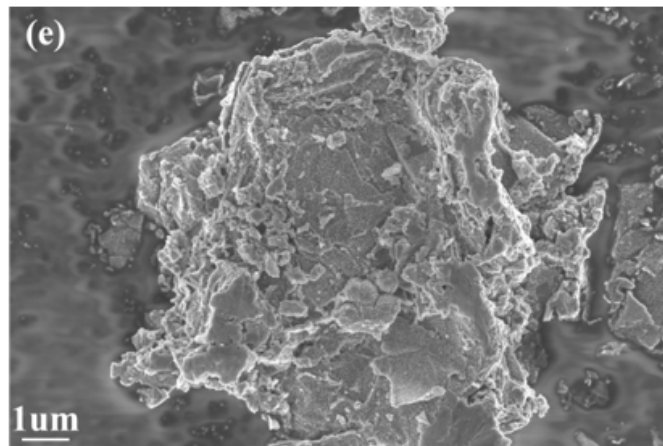
(a) TEM image of RGO-MoS$_2$ (500 nm)
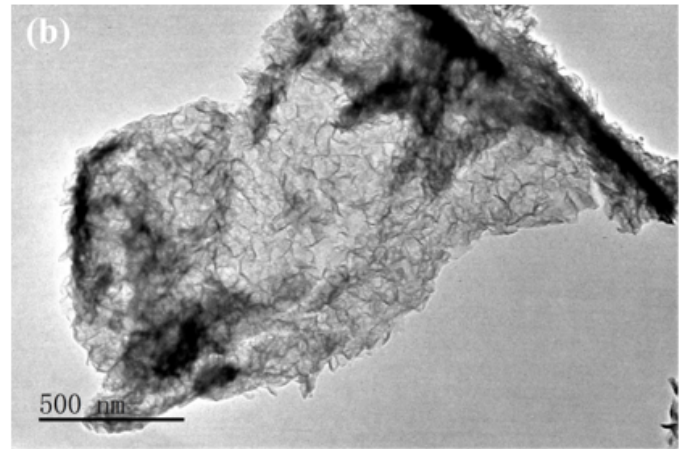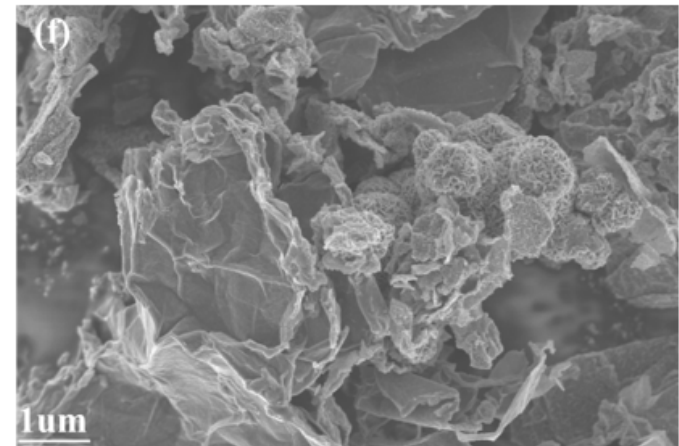
(b) TEM image of OA-RGO-MoS$_2$ (500 nm)
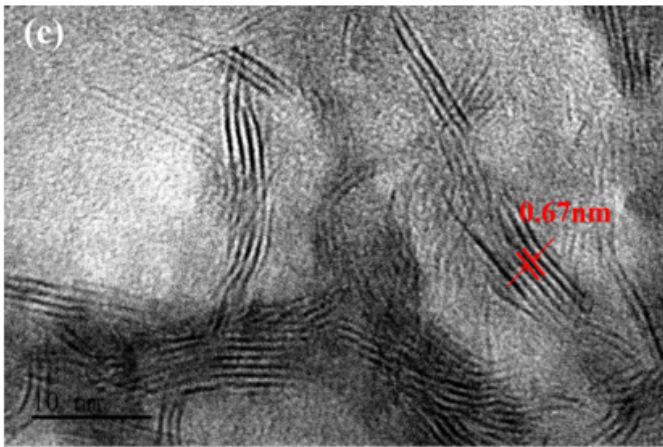
(c) HRTEM image of RGO-MoS$_2$ (10 nm)

(d) HRTEM image of OA-RGO-MoS$_2$ (10 nm)

(e) SEM image of RGO-MoS$_2$ (1 μm)

(f) SEM image of OA-RGO-MoS$_2$ (1 μm)
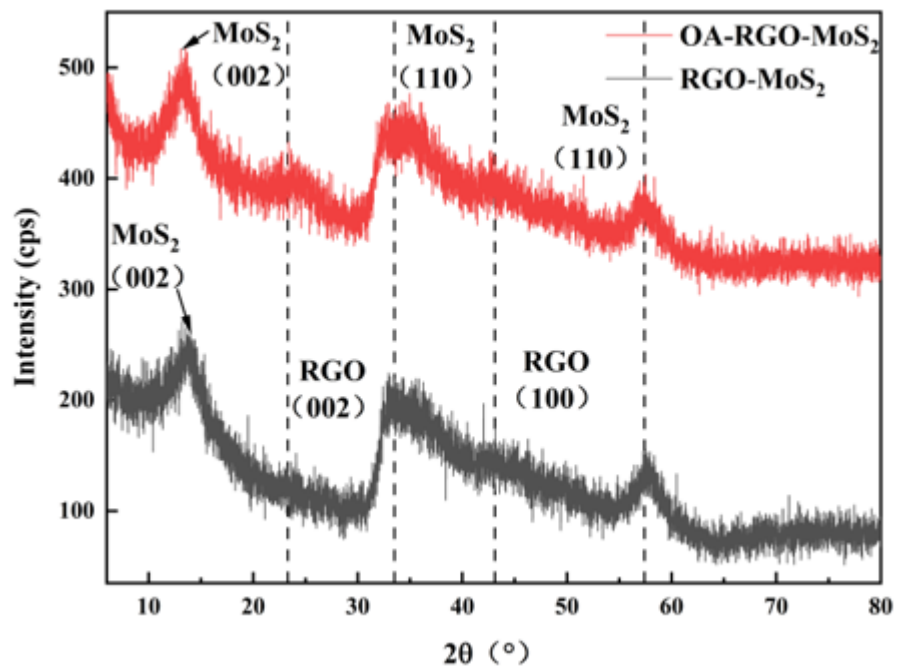
Figure 2

Morphology of RGO-MoS2 and OA-RGO-MoS2

Figure 3

XRD pattern of RGO-MoS2 and OA-RGO-MoS2
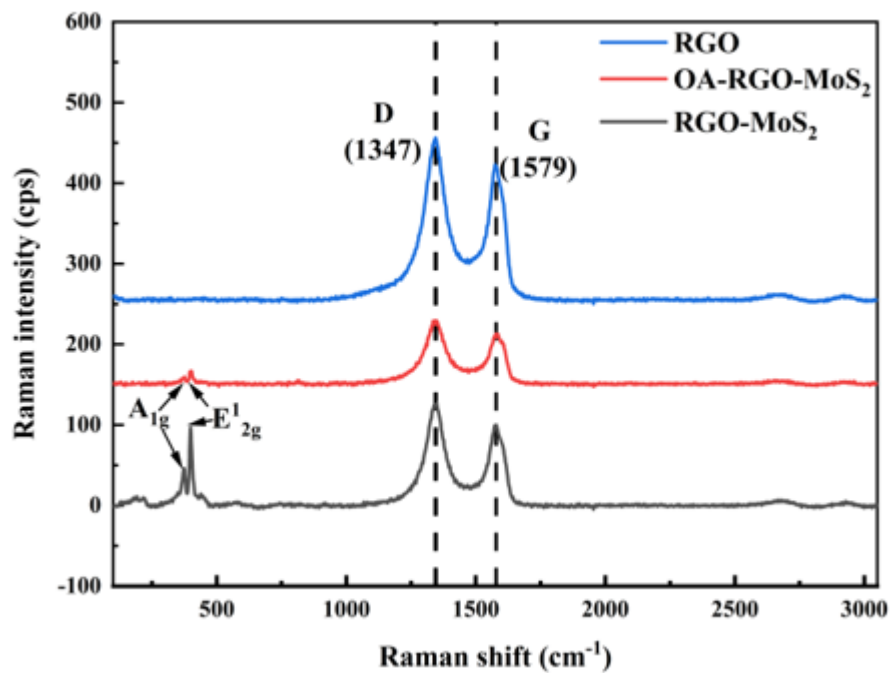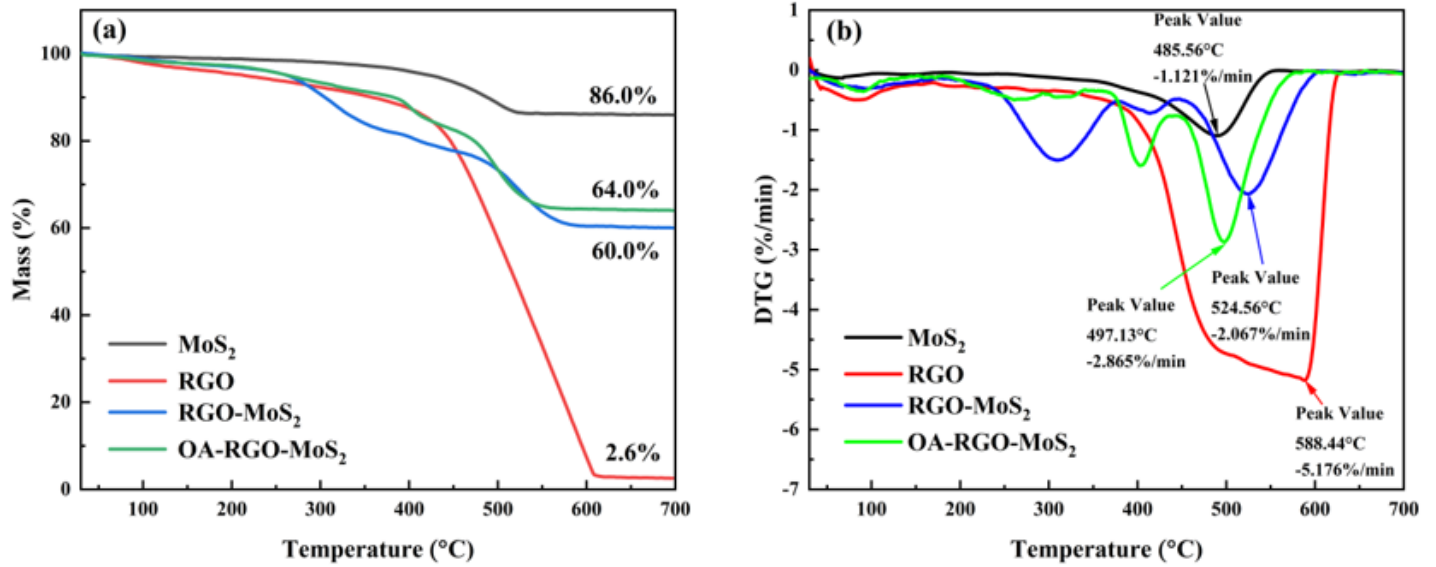

Figure 4

Raman pattern of RGO, RGO-MoS2 and OA-RGO-MoS2

Figure 5

The TGA (a) and DTG (b) curves of RGO and RGO-MoS2 and OA-RGO-MoS2
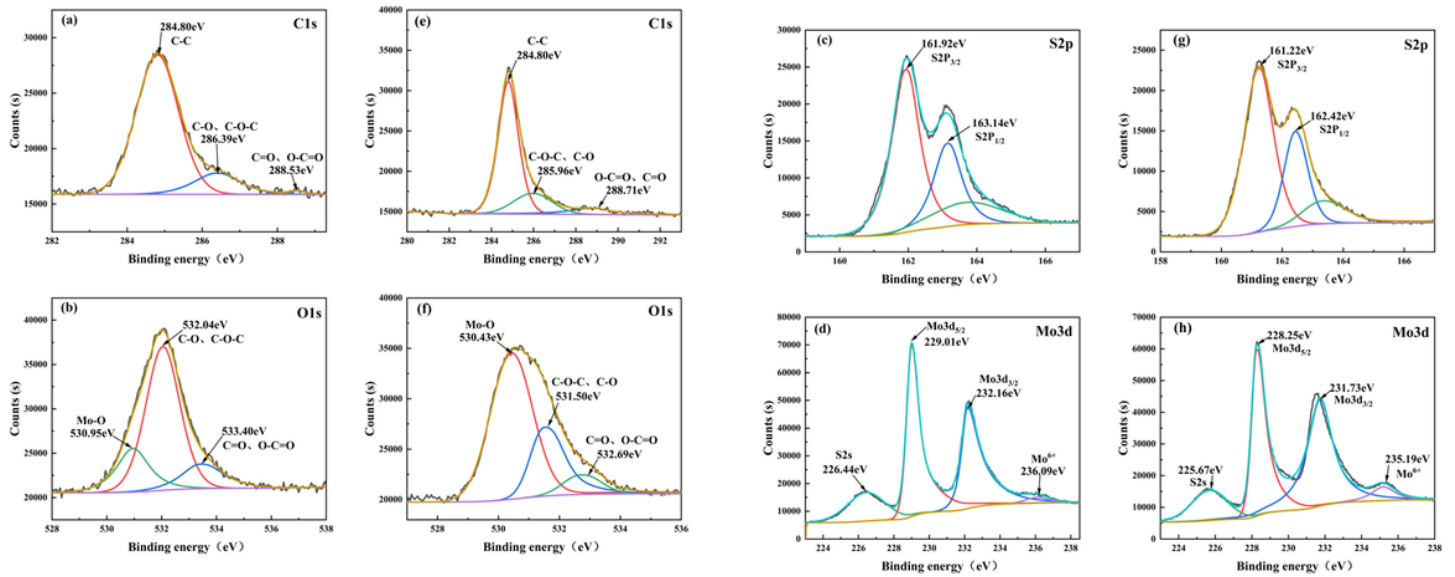
Figure 6

XPS spectra of RGO-MoS2 (a、b、c、d) and OA-RGO-MoS2 (e、f、g、h)
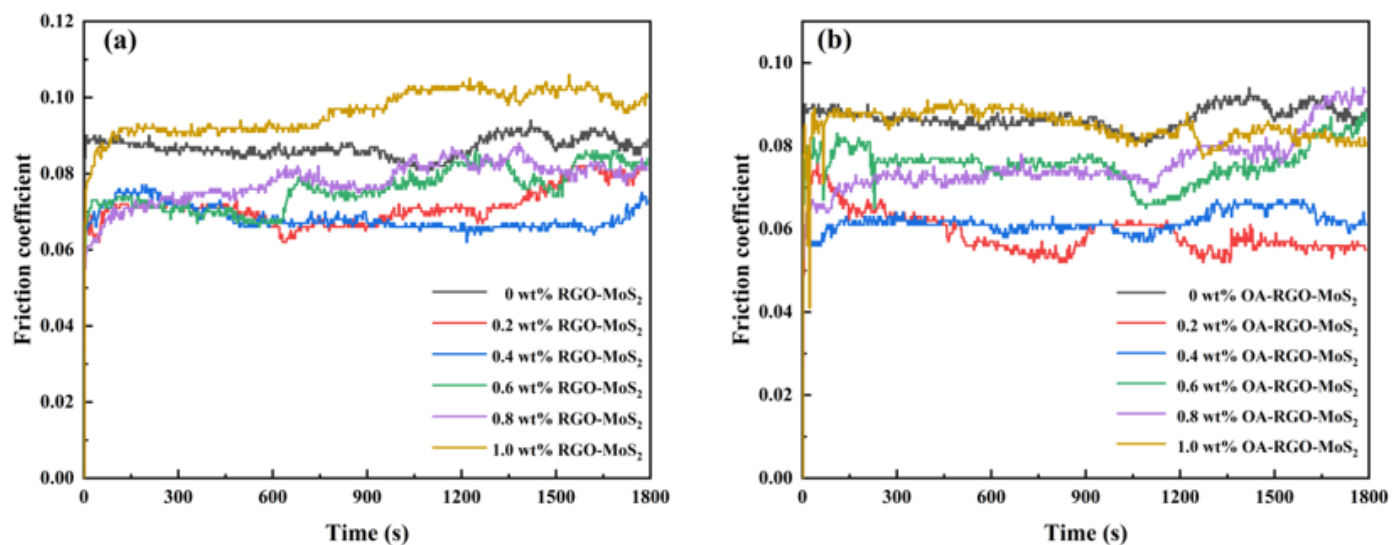
Figure 7

Friction coefficient of RGO-MoS2 (a) and OA-RGO-MoS2 (b)
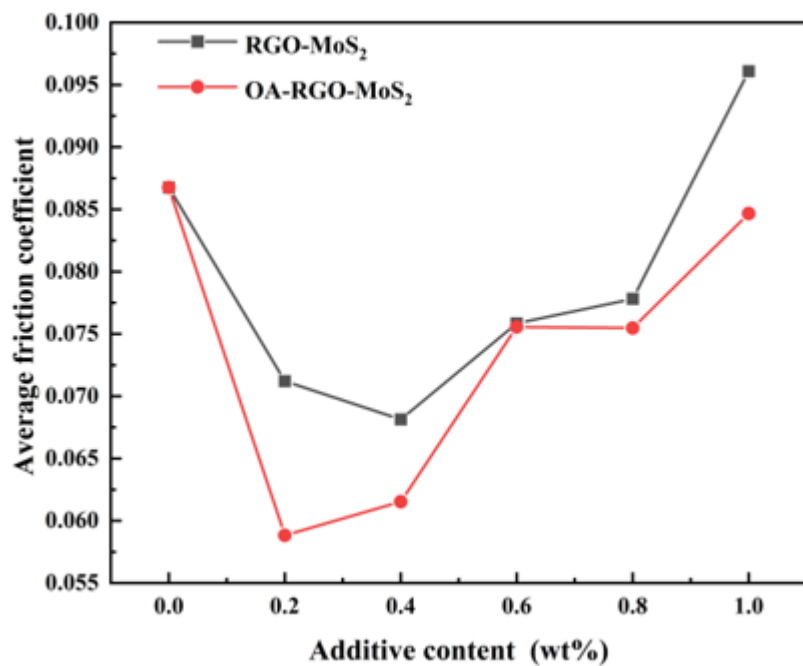
Figure 8

Average friction coefficient of RGO-MoS2 and OA-RGO-MoS2
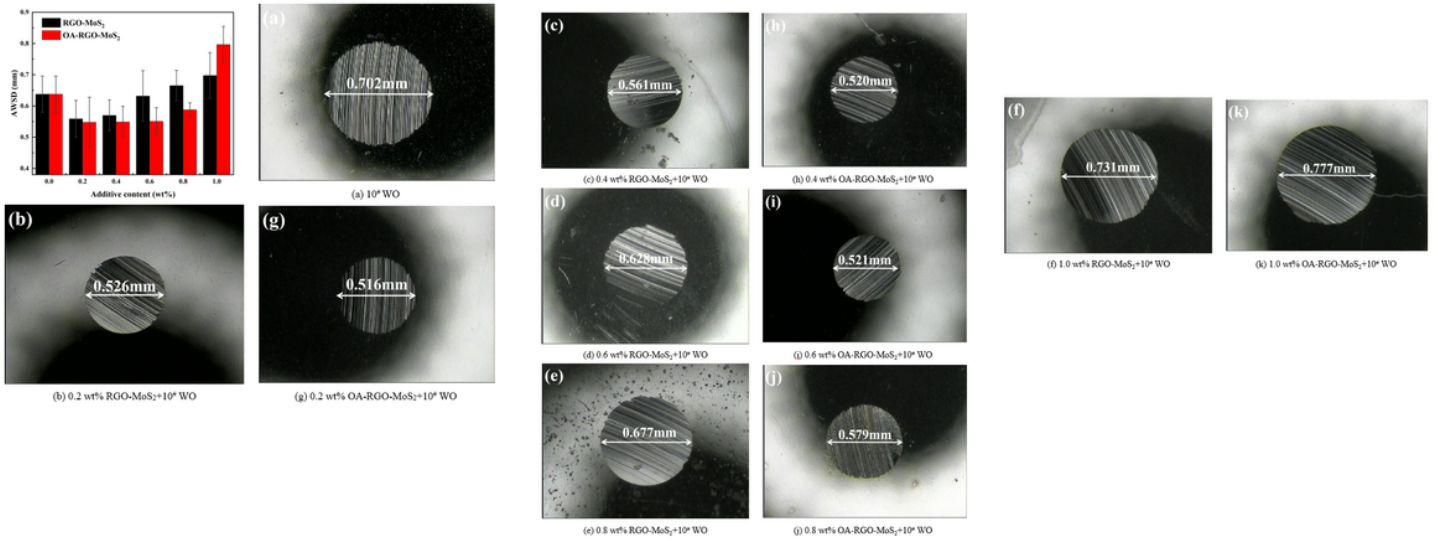
Figure 9

The morphology of the down test ball (a-k) of RGO-MoS2 and OA-RGO-MoS2 and the variation trend of the mean scar diameter of the down test ball
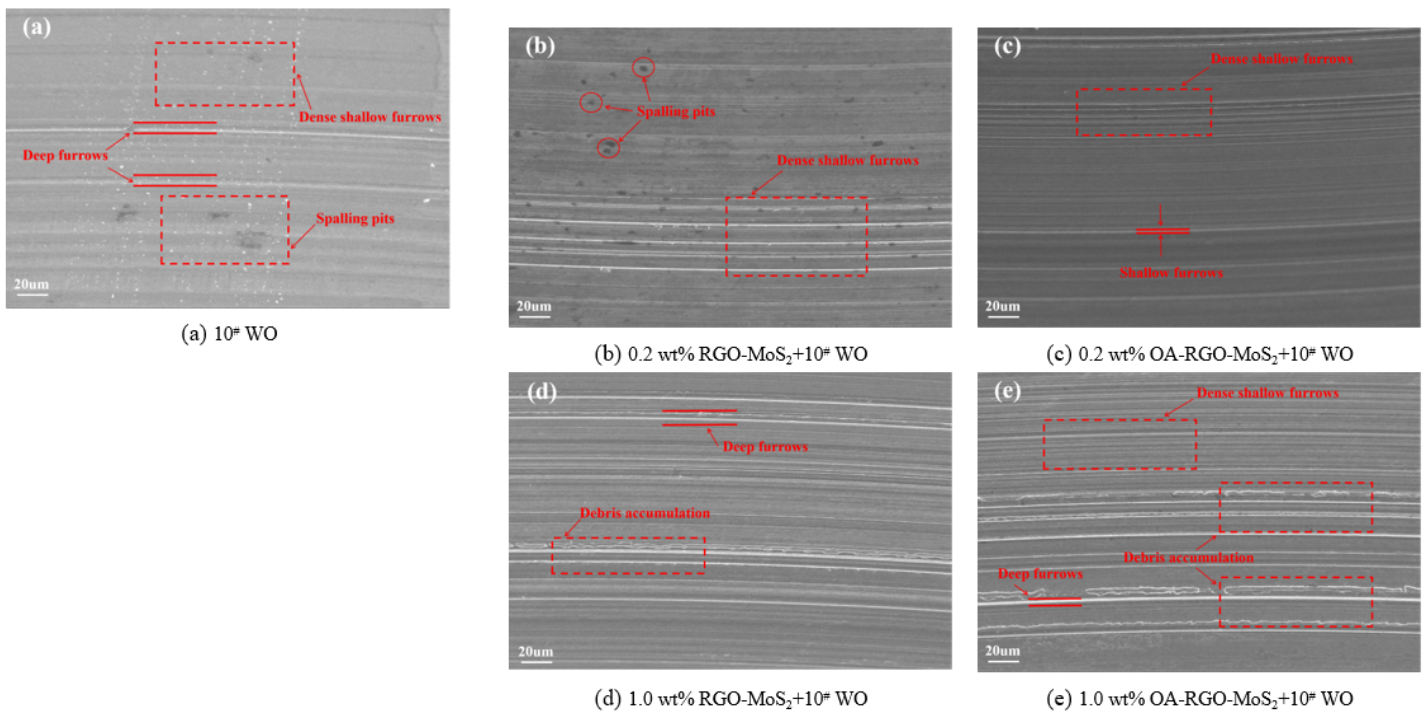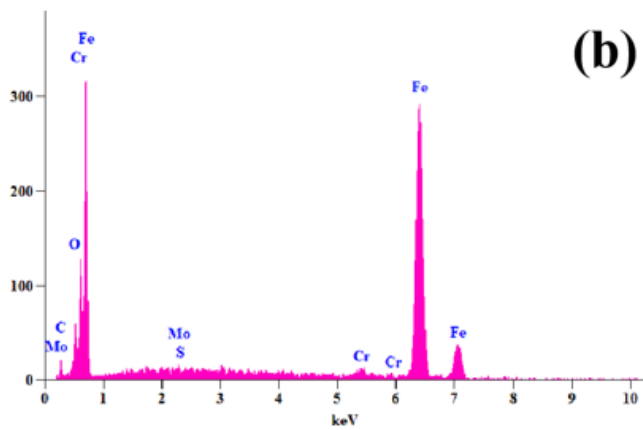

Figure 10

SEM topography photo of wear scar surface of upper test ball
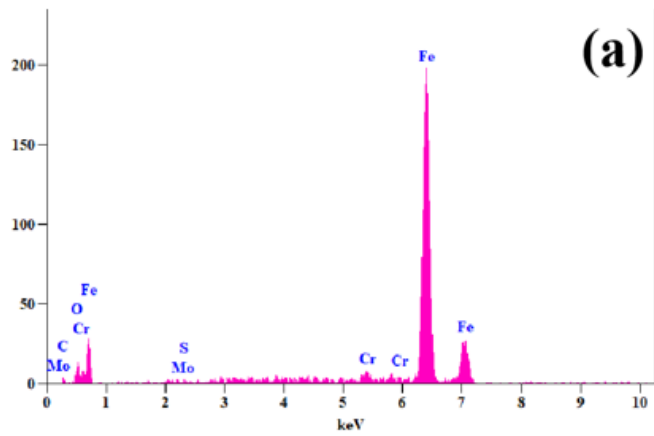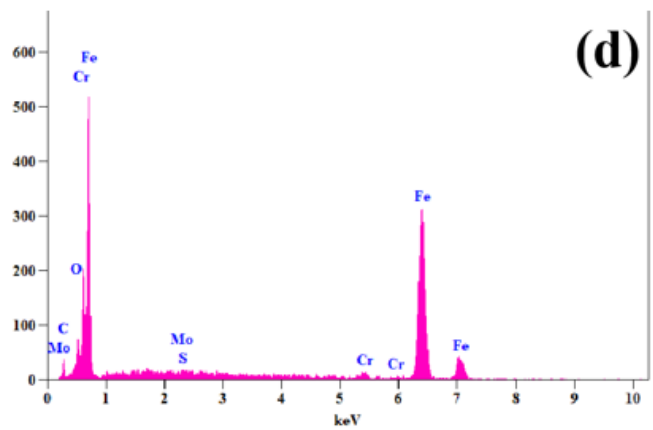
(a) 0.2 wt% RGO-MoS₂+10# WO
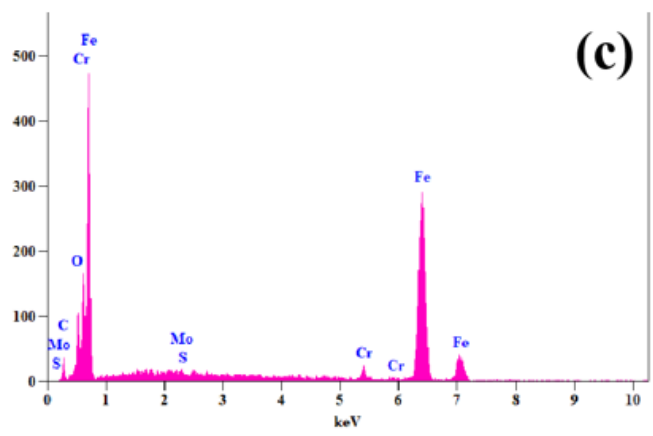
(b) 0.2 wt% OA-RGO-MoS₂+10# WO

(c) 1.0 wt% RGO-MoS₂+10# WO

(d) 1.0 wt% OA-RGO-MoS₂+10# WO

Figure 11

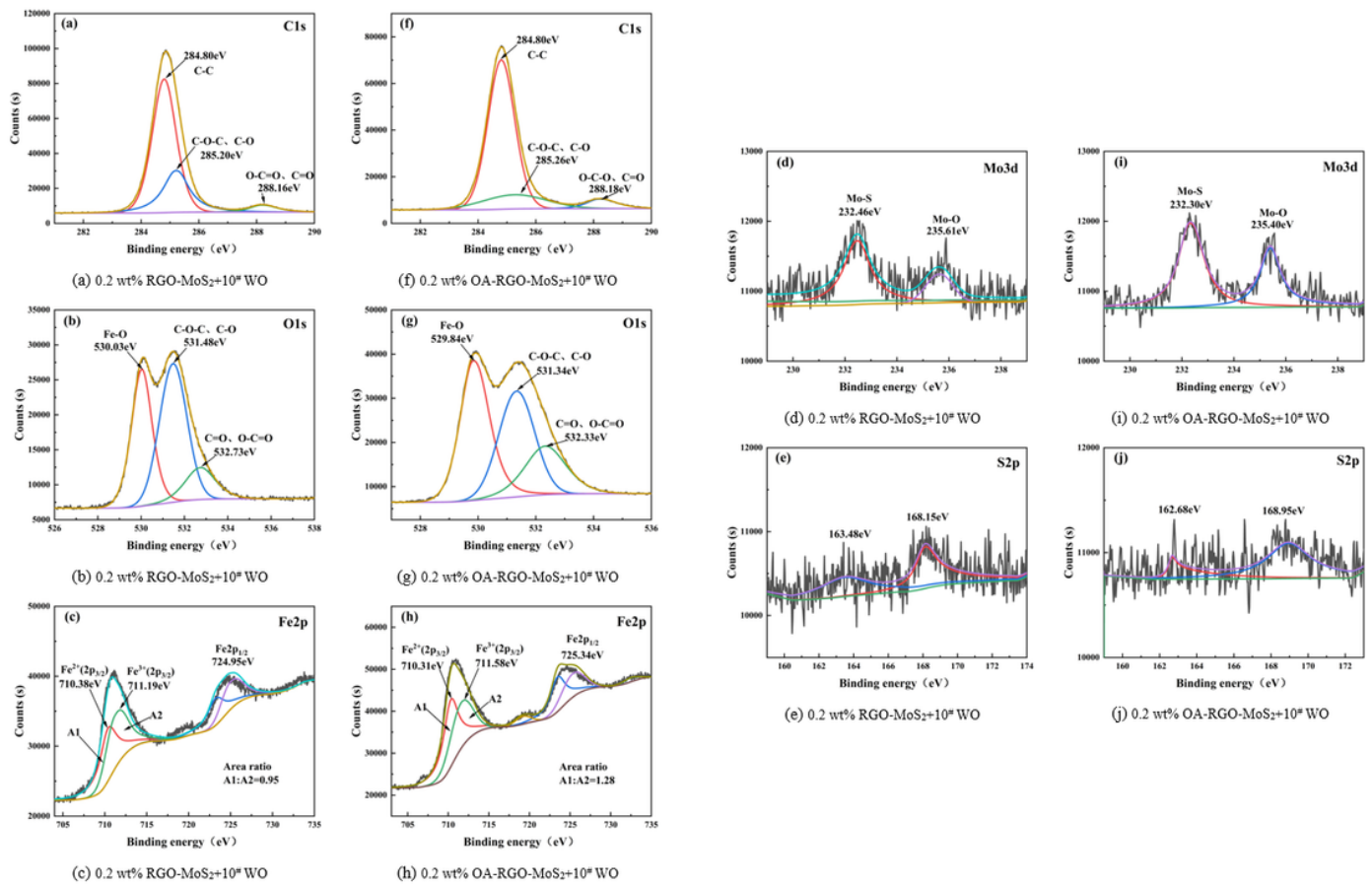EDS spectrum of the wear scar surface of the upper test ball

Figure 12

XPS diagram of ball wear marks on RGO-MoS2 (a、b、c、d、e) and OA-RGO-MoS2 (f、g、h、i、j)